Sixth International Symposium on Turbulence and Shear Flow Phenomena
Seoul, Korea, 22-24 June 2009

IMPLICIT LARGE-EDDY SIMULATION OF PASSIVE-SCALAR MIXING IN A RECTANGULAR-JET REACTOR

Antoine Devesa, Stefan Hickel and Nikolaus A. Adams
Institute of Aerodynamics,
Technische Universität München, Boltzmannstraße 15, 85748 Garching, Germany
antoine.devesa@aer.mw.tum.de

INTRODUCTION

The subgrid-scale (SGS) modeling environment provided by the Adaptive Local Deconvolution Method (ALDM) has been recently extended to Large-Eddy Simulations (LES) of passive-scalar transport. The resulting adaptive advection algorithm has been described and discussed with respect to its numerical and turbulence-theoretical background in Hickel et al. (2007). Results demonstrate that this method allows reliable predictions of the turbulent transport of passive-scalars in isotropic turbulence and in turbulent channel flow from small to moderate Schmidt numbers. Due to the strong influence of the molecular Schmidt number Sc on the Batchelor characteristic scales, difficulties in the modeling of the passive-scalar transport arise when the diffusive structures are several order of magnitude smaller than the viscous scales ($Sc \gg 1$). In this paper, we present the results from implicit LES of the flow in a confined rectangular-jet reactor and an analysis of the mixing of a passive-scalar with high Schmidt number: $Sc = 1,250$. The numerical study is carried out in collaboration with experimentalists from Iowa State University.

IMPLICIT LES

We consider LES of turbulent flows which are governed by the Navier-Stokes equations and by the incompressible continuity equation. A finite-volume discretization is obtained by convolution with the top-hat filter $\boldsymbol{G}$:

$$\frac{\partial \bar{\boldsymbol{u}}_N}{\partial t} + \boldsymbol{\nabla} \cdot \bar{\boldsymbol{N}}_N(\boldsymbol{u}_N) - \nu \boldsymbol{\nabla} \cdot \boldsymbol{\nabla} \bar{\boldsymbol{u}}_N = -\boldsymbol{\nabla} \cdot \bar{\boldsymbol{\tau}}_{SGS} \quad (1)$$

$$\boldsymbol{\nabla} \cdot \bar{\boldsymbol{u}}_N = 0 \quad (2)$$

where an overbar denotes the filtering $\bar{\boldsymbol{u}} = \boldsymbol{G} * \boldsymbol{u}$. The nonlinear term is abbreviated as $\boldsymbol{\nabla} \cdot \boldsymbol{N}(\boldsymbol{u}) = \boldsymbol{\nabla} \cdot \boldsymbol{u}\boldsymbol{u} + \boldsymbol{\nabla} p$, where $\boldsymbol{u}$ is the velocity field and p is the pressure. The employed filter approach by Leonard (1974) implies a subsequent discretization of the filtered equations. The subscript N indicates the resulting grid functions obtained by projecting continuous functions on the numerical grid. This projection corresponds to an additional filtering in Fourier space with a sharp cut-off at the Nyquist wavenumber $\xi_C = \pi/h$, where h is a constant grid spacing. The subgrid-stress tensor:

$$\boldsymbol{\tau}_{SGS} = \boldsymbol{N}(\boldsymbol{u}) - \boldsymbol{N}_N(\boldsymbol{u}_N) \quad (3)$$

originates from the discretization of the non-linear terms and has to be modeled in order to close Eq. (2). To certain extents, common explicit models are based on sound physical theories. Solved numerically, however, the discrete approximation of the explicit SGS model competes against the truncation error of the underlying numerical scheme. A theoretical analysis performed by Ghosal (1996) comes to the conclusion that even a fourth-order central difference discretization has a numerical error which can have the same order of magnitude as the SGS model. This fact is exploited for implicit large-eddy simulation where no SGS model terms are computed explicitly. Rather the truncation error of the numerical scheme is used to model the effects of unresolved scales. A recent review on previous implicit LES approaches is provided, e.g. by Grinstein and Fureby (2004).

The Modified Differential Equation (MDE) for an implicit LES scheme is given by:

$$\frac{\partial \bar{\boldsymbol{u}}_N}{\partial t} + \widetilde{\boldsymbol{G}} * \widetilde{\boldsymbol{\nabla}} \cdot \widetilde{\boldsymbol{N}}_N(\widetilde{\boldsymbol{u}}_N) - \nu \boldsymbol{\nabla} \cdot \boldsymbol{\nabla} \bar{\boldsymbol{u}}_N = \boldsymbol{0} \quad (4)$$

$$\boldsymbol{\nabla} \cdot \bar{\boldsymbol{u}}_N = 0 \quad (5)$$

where $\widetilde{\boldsymbol{u}}_N$ denotes an approximant of the velocity $\boldsymbol{u}_N$. The local Riemann problem is solved by a consistent numerical flux function $\widetilde{\boldsymbol{N}}_N$. The symbols $\widetilde{\boldsymbol{G}}$ and $\widetilde{\boldsymbol{\nabla}}$ indicate that $\boldsymbol{G}$ and $\boldsymbol{\nabla}$ are replaced by their respective numerical approximations. In fact $\widetilde{\boldsymbol{G}} * \widetilde{\boldsymbol{\nabla}}$ can be a nonlinear operator. The truncation error is accordingly:

$$\boldsymbol{\mathcal{G}}_N = \boldsymbol{G} * \boldsymbol{\nabla} \cdot \boldsymbol{N}_N(\boldsymbol{u}_N) - \widetilde{\boldsymbol{G}} * \widetilde{\boldsymbol{\nabla}} \cdot \widetilde{\boldsymbol{N}}_N(\widetilde{\boldsymbol{u}}_N) \quad (6)$$

For implicit SGS modeling the discretization scheme is specifically designed so that the truncation error $\boldsymbol{\mathcal{G}}_N$ has physical significance, i.e.:

$$\boldsymbol{\mathcal{G}}_N \approx -\boldsymbol{G} * \boldsymbol{\nabla} \cdot \boldsymbol{\tau}_{SGS} \quad (7)$$

THE ALDM APPROACH

With the adaptive local deconvolution method (ALDM) the local approximation $\widetilde{\boldsymbol{u}}_N$ is obtained from a solution-adaptive combination of deconvolution polynomials. Numerical discretization and SGS modeling are merged entirely. This is possible by exploiting the formal equivalence between cell-averaging and reconstruction in finite-volume discretizations and top-hat filtering and deconvolution in SGS-modeling. Instead of maximizing the order of accuracy, deconvolution is regularized by limiting the degree of local interpolation polynomials and by permitting lower-order polynomials to contribute to the truncation error. Adaptivity of the deconvolution operator is achieved by weighting the respective contributions by an adaptation of WENO smoothness measures (Shu, 1997). The approximately deconvolved field is inserted into a consistent numerical flux function. Flux function and nonlinear weights introduce free parameters. These allow the control of the truncation error which provides the implicit SGS model.

The performance of the optimized implicit model was evaluated by simulations of different flow configurations. Large-scale forced and decaying three-dimensional homogeneous isotropic turbulence were considered at a wide range of Reynolds numbers. For transitional flows the model performance was tested on the simulation of the instability and

breakdown of the 3D Taylor-Green vortex. For all test cases the implicit model shows an excellent agreement with theory and experimental data. It is demonstrated that ALDM performs at least as well as established explicit models (Hickel et al., 2006).

IMPLICIT SUBGRID-SCALE MODELING FOR PASSIVE-SCALAR TRANSPORT

We consider the turbulent transport of passive-scalars, which do not measurably affect the velocity field. This case represents a one-way coupling of the scalar to the fluid. Hence, the closure problem is restricted to the scalar transport equation, where the flux function $\mathbf{F}$ is formally linear in c:

$$\frac{\partial c}{\partial t} + \nabla.\mathbf{F}(\mathbf{u}, c) = 0 \quad \text{with:} \quad \mathbf{F}(\mathbf{u}, c) = \mathbf{u}c - \frac{1}{ReSc}\nabla c \quad (8)$$

Turbulence modeling and discretization for the momentum equations remain unchanged (Hickel et al., 2006). However, the evolution of a non-uniform scalar field is subject to the velocity dynamics. Small-scale fluctuations of velocity and scalar are correlated in the presence of a scalar concentration gradient. The projection of Eq. (8) on a grid with finite resolution results in the modified equation:

$$\frac{\partial c_N}{\partial t} + \nabla.\mathbf{F}_N(\mathbf{u}_N, c_N) = \tau_{SGS} \quad (9)$$

The subgrid tensor: $\tau_{SGS} = \mathbf{F}(\mathbf{u}, c) - \mathbf{F}_N(\mathbf{u}_N, c_N)$ originates from the grid projection of advective terms and represents the effect of the action of subgrid scales and has to be approximated by a SGS model.

The various regimes (Fig. 1) that exist for the variance spectrum of passive-scalars at different Schmidt numbers (Batchelor, 1959) have to be recovered by the SGS model. In the ALDM framework, implicit SGS modeling is accomplished by calibrating free discretization parameters. An analysis of the typical wave numbers, for low Schmidt number and high Schmidt number scalars, revealed that different parameters are required for each of these regimes. This approach for passive-scalar mixing has already been validated for several canonical flows by Hickel et al. (2007). The computation of the experimental setup presented here will then assess the high Schmidt number model in a complex configuration.

EXPERIMENTAL SETUP

The mixing of very high Schmidt number passive-scalars was recently studied under the conditions of laboratory experiments by the group of Rodney Fox at Iowa State University (Feng, 2006).

In this experiment, a confined coplanar jet configuration is investigated, where the flow is seeded by Rhodamine particles, representing a passive-scalar with a Schmidt number of $Sc = 1,250$. A non-scaled three-dimensional sketch of this test rig is displayed in Fig. 2. The shear flow is generated through out three inlet channels of identical height ($d = 20\ mm$), separated by two splitter plates, with a liquid phase flowing at different velocities. Free stream velocities are 0.5, 1.0, and 0.5 m/s in the top, center and bottom inlet channels respectively, corresponding to a Reynolds number of $Re = 50,000$, based on the distance d and the velocity difference between central and lateral channels.

The measurements are carried out in a Plexiglas test section with a rectangular cross-section measuring 60 mm (height) by 100 mm (width) and with an overall length of 1 m, so that the aspect ratio height:width for each inlet channel is 1:5. Particle Image Velocimetry (PIV) is used to measure the instantaneous velocity field in five planar cross sections of the observed flow, corresponding to the five stations, S1 to S5, at $x/d = 1$, $x/d = 4.5$, $x/d = 7.5$, $x/d = 12$ and $x/d = 15$ respectively. Scalar concentration measurements are carried out simultaneously at the same locations using Planar Laser-Induced Fluorescence (PLIF), so that velocity-scalar correlations can be computed. A experimental database was then generated, including first- and second-order moments for velocity and scalar concentration, as well as cross-correlations. For further details of the experimental configuration, please refer to the latest publications of the group on this topic by Feng et al. (2005) and Feng (2006).

In close collaboration with the experimentalists and in the framework of the validation and assessment of the previously presented implicit LES approach, we perform implicit LES of the mixing and transport of a passive-scalar in this confined rectangular-jet reactor configuration. In the following section, some details of the numerical setup are given.

COMPUTATIONAL DETAILS

The flow is described by the incompressible Navier-Stokes equations, that are discretized on a staggered Cartesian mesh. For time advancement, the fractional step method with an explicit third-order Runge-Kutta scheme is used. The time-step is dynamically adapted to satisfy a Courant-Friedrichs-Lewy condition with $CFL = 1.0$. The pressure-Poisson equation and diffusive terms are discretized by second-order centered differences. The convective terms of the momentum and passive-scalar transport equations are discretized by the ALDM, which also provides a SGS model. The Poisson solver employs the stabilized Bi-Conjugate Gradient (BiCGstab) method. The presented results are obtained by the Simplified Adaptive Local Deconvolution (SALD) algorithm (Hickel and Adams, 2006) which is an implementation of the implicit LES method ALDM with improved computational efficiency (Hickel et al. 2006).

The computational domain is divided into two parts. The inlet is composed of three channels, one in the center and two lateral ones, where the bulk velocity is twice as low. The three channels are periodic in stream- and spanwise directions, while bounded by solid walls in the transverse direction. The measurement section of the domain is confined by side walls in spanwise and transverse directions, while inflow conditions are taken from the inlet channels. The computational domain has a total extent of $60d \times 3d \times 5d$ and is discretized by 14.4×10^6 finite volumes.

NUMERICAL RESULTS

In this section, the main results obtained from the implicit LES are presented and compared to the measurements.

A qualitative analysis is first undertaken. Fig. 3 shows instantaneous velocity (left) and scalar concentration (right) fields from the implicit LES. The three inlet channels (bottom) and the long reactor part (long upper part) of the computational domain can be identified on these snapshots. The jet expansion close to the splitter plates and its further development downstream towards a flat channel flow are observed. The two mixing layers generated by the splitter plates reach a stable position after approximately $x/d = 10$,

due to the confinement between the top and bottom walls.

A further analysis is concerned with the comparison between experimental data and numerical results. Since the flow is confined in the spanwise direction as well, there is no homogeneous direction at all in this configuration. The numerical quantities presented here are hence only temporal statistics over about 1800 samples, and no spatial averaging is used. Despite this high number of samples, the statistics appear to be not totally smooth for some second-order moments. Among the five available observation positions of the experimental setup, only three are analyzed in the following: S1 ($x/d = 1$), S3 ($x/d = 7.5$) and S5 ($x/d = 15$).

Figs. 4 and 5 depict the comparison between experimental data and numerical results based on the averaged streamwise velocity and scalar concentration respectively. The flow topology and expansion of the jet are found to be in agreement with the experiment. First order moments for both dynamics and passive-scalar concentration from the implicit LES match globally very well with the experimental data. Indeed, comparisons at the two other measurement stations of the test rig exhibit the same concordance.

The main challenge of this work is, however, the comparison of second-order moments. Even though the flow-dynamic quantities, namely the streamwise and cross-stream Reynolds stresses, as well as the shear-stress, are not presented here for the sake of concision, numerical results were found to match satisfactorily the measured data. The two peaks of scalar concentration variance (Fig. 6) at the first observation station S1 shows the high mixing regions corresponding to the position of the splitter plates. At this station, the resolution in the experiment is not sufficient to capture the real amplitude of those peaks. Therefore we think that the discrepancy with the implicit LES is not dramatic at this position. Further downstream, where the mixing is weaker, both numerical and experimental data agree quite well.

A further analysis is concerned with the velocity-scalar concentration correlations, that experimentalists could measure using simultaneously PIV / PLIF acquisition chains. Both correlations $< u'c' >$ and $< v'c' >$ have been normalized by the rms velocity and scalar concentration fluctuations, yielding to the velocity-concentration correlation coefficients:

$$< u'c' >_N = \frac{< u'c' >}{< u' >_{rms} < c' >_{rms}} \tag{10}$$

$$< v'c' >_N = \frac{< v'c' >}{< v' >_{rms} < c' >_{rms}} \tag{11}$$

The comparison of both quantities with the numerical results is shown in Figs. 7 and 8 and demonstrate an almost perfect agreement. The key-features of the flow present in the experiment are found in the simulation as well. At the closest position to the splitter plate S1, scalar concentration and velocity are totally uncorrelated in the core regions of the three inlet channels, giving levels close to 0. The longitudinal coefficient (Fig. 7) exhibits two separated high correlation regions, in the whole confined reactor, even if at S5, these regions almost take the form of two plateaus. The lateral coefficient (Fig. 8) is antisymmetric and the amplitudes in the zones of high correlation remain quite the same along the observation domain.

From the turbulent fluxes, the resolved turbulent viscosity and diffusivity can be computed, based on the assumption that the turbulent fluxes are proportional to the velocity or scalar concentration gradients (Batchelor, 1949). These proportionality ratios are such that:

$$\nu_T = \frac{- < u'v' >}{\partial U/\partial y} \tag{12}$$

$$\Gamma_{22} = \Gamma_T = \frac{- < v'c' >}{\partial c/\partial y} \tag{13}$$

where the subscript 22 corresponds to the component (2,2) of the turbulent diffusivity tensor, which is not diagonal in this case, since the mean scalar concentration gradient is not aligned with the turbulent flux vector. The profiles are shown in Figs. 9 and 10. The agreement between experiment and simulation is once again very satisfactory, and the main features of the flow are recovered, even if the results at the station S1, the closest one to the splitter plates, are not appropriate for an analysis. Indeed, due to the presence of the division by the velocity or scalar concentration gradient respectively, these profiles show non-physical peaks. However, at S3 and S5, the maxima appear always at the location of the shear-layers, whereas these quantities tend to 0 close to the top and bottom walls. The amplitudes of the resolved part of the turbulent viscosity ν_T are in good agreement with the experiment for the stations upstream, but not perfectly recovered at the furthest one, S5. The trend for the turbulent diffusivity Γ_T is opposite: the prediction of the implicit LES is better far from the splitter plates as at the first stations S1 and S3.

A measure of the turbulent Schmidt number can consequently be estimated:

$$Sc_T = \frac{\nu_T}{\Gamma_T} \tag{14}$$

The most classical subgrid-scale is based on the assumption of a constant turbulent Schmidt number of the order of 1. The results show that this assumption could hold, in this case, far away from the high mixing regions, but not in the intense shear and transport regions. In those places, the turbulent Schmidt number can clearly exhibit variations of more than several hundreds percent from a constant Schmidt number assumption ($Sc_T \approx 1$). Indeed, experimental values for the turbulent Schmidt number were for instance around 4 at the station S3, in the both shear-layers. Numerical values at these places were however remained in a smaller range of variation from the constant turbulent Schmidt number hypothesis.

Other relevant quantities for the modeling of the passive-scalar transport, such as the other component of the turbulent diffusivity tensor

$$\Gamma_{12} = \frac{- < u'c' >}{\partial c/\partial y} \tag{15}$$

were measured experimentally and the corresponding implicit LES results agreed satisfactorily with them. These are not presented here for concision but will be discussed during the TSFP6 presentation.

CONCLUSION

In this paper, the numerical results from an implicit LES of the mixing of a passive-scalar ($Sc = 1,250$) in a confined coplanar reactor configuration are presented and analyzed. The agreement with experimental data for first- and second-moments is very satisfactory in the whole measurement region of the experiment. Some relevant quantities for the modeling of the passive-scalar transport equation, such as the resolved turbulent viscosity and diffusivity, are

computed and described, as well as the turbulent Schmidt number. The very good overall agreement between experiment and simulation validates the presented implicit LES modeling environment for passive-scalars at high Schmidt numbers.

REFERENCES

Batchelor, G.K., 1949, "Diffusion in a field of homogeneous turbulence", *Australian J. of Scientific Research A*, Vol. 2, pp. 437-450.

Batchelor, G.K., 1959, "Small-scale variation of convected quantities like temperature in turbulent fluid. Part 1. General discussion and the case of small conductivity", *J. Fluid Mech.*, Vol. 5, pp. 113-133.

Feng, H., 2006, *Experimental study of turbulent mixing in a rectangular reactor*, Ph.D. Thesis, Iowa State University, Ames, Iowa.

Feng, H., Olsen, M.G., Liu, Y., Fox, R.O., and Hill, J.C., 2005, "Investigation of turbulent mixing in a confined planar-jet reactor". *AIChE J.*, Vol. 51, pp. 2649-2664.

Ghosal, S., 1996, "An analysis of numerical errors in Large-Eddy Simulations of turbulence", *J. Comput. Phys.*, Vol. 125, pp. 187-206.

Grinstein, F.F., and Fureby, C., 2004, "From canonical to complex flows: recent progress on monotonically integrated LES", *Comp. Sci. Eng.*, Vol. 6, pp. 36-49.

Hickel, S., Adams, N.A., and Domaradzki, J.A., 2006, "An adaptive local deconvolution method for implicit LES", *J. Comput. Phys.*, Vol. 213, pp. 413-436.

Hickel, S., Adams, N.A., and Mansour, N.N., 2007, "Implicit subgrid-scale modeling for Large-Eddy Simulation of passive-scalar mixing", *Phys. Fluids*, Vol. 19, Nr. 095102.

Leonard, A., 1974, "Energy cascade in Large-Eddy Simulations of turbulent fluid flows", *Adv. Geophys.*, Vol. 18A, pp. 237-248.

Shu, C.-W., 1997, "Essentially non-oscillatory and weighted essentially non-oscillatory schemes for hyperbolic conservation laws", *Tech. Rep. 97-65*, ICASE, NASA Langley Research Center, Hampton, Virginia.

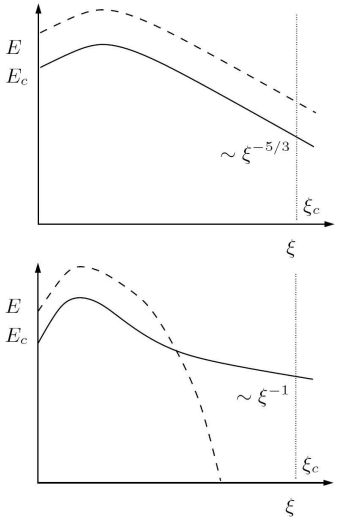

Figure 1: Critical test cases for predicting the proper subgrid diffusion in Large-Eddy Simulations of scalar mixing. *Top:* Low Schmidt number regime. *Bottom:* High Schmidt number regime at moderate Reynolds number. ——— scalar variance; – – – – kinetic energy; · · · · · numerical cutoff wavenumber

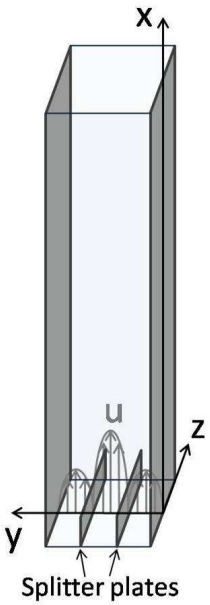

Figure 2: Sketch of the experimental setup (for the sake of clarity, the front and back walls are not depicted)

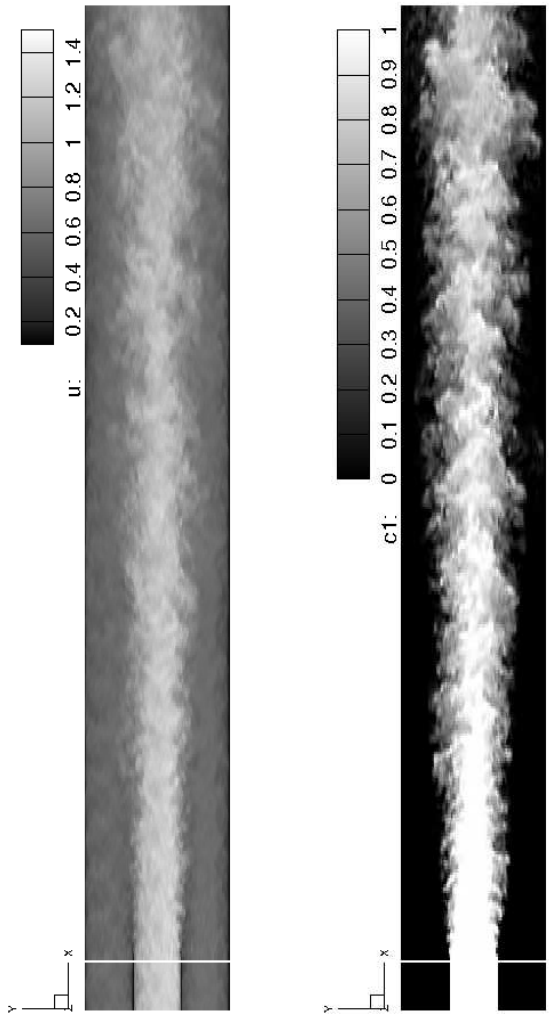

Figure 3: Snapshot of the streamwise velocity (left) and scalar concentration (right) fields

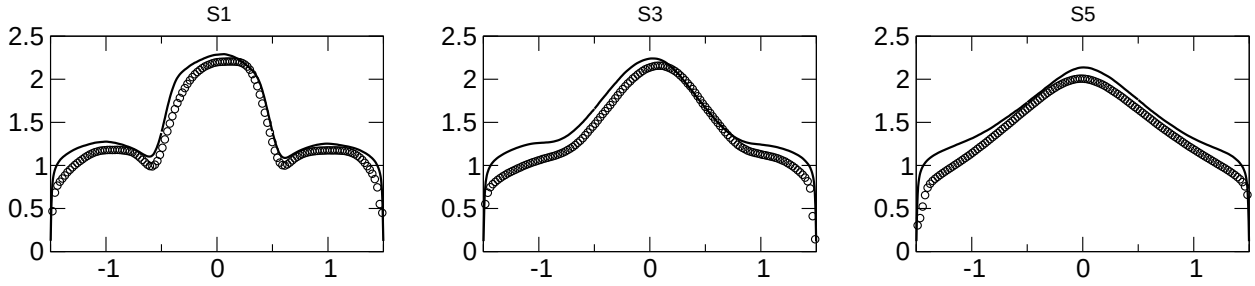

Figure 4: Mean streamwise velocity profiles at 3 measurement stations. Symbols: experiment; solid line: implicit LES

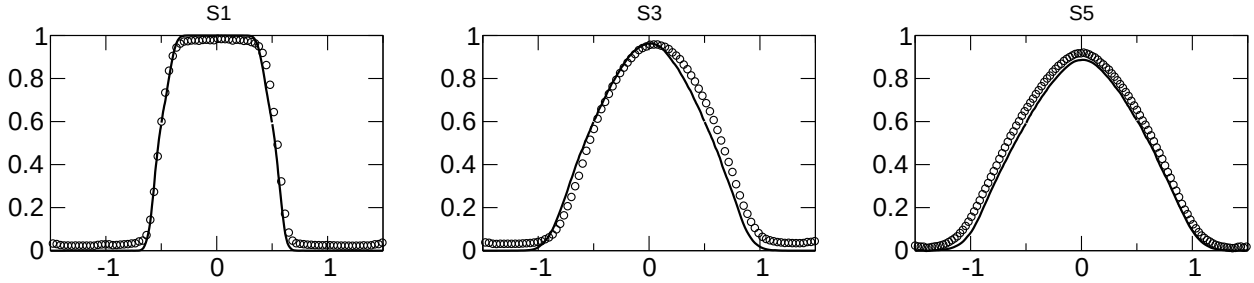

Figure 5: Mean scalar concentration profiles at the 3 measurement stations. Symbols: experiment; solid line: implicit LES

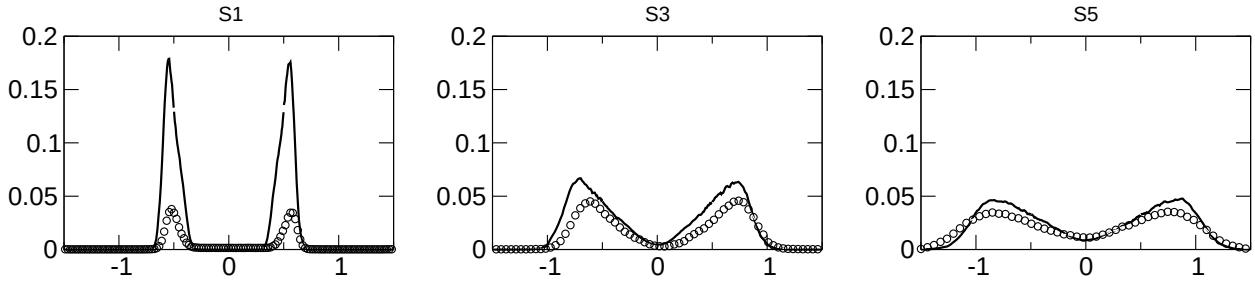

Figure 6: Scalar variance at the 3 measurement stations. Symbols: experiment; solid line: implicit LES

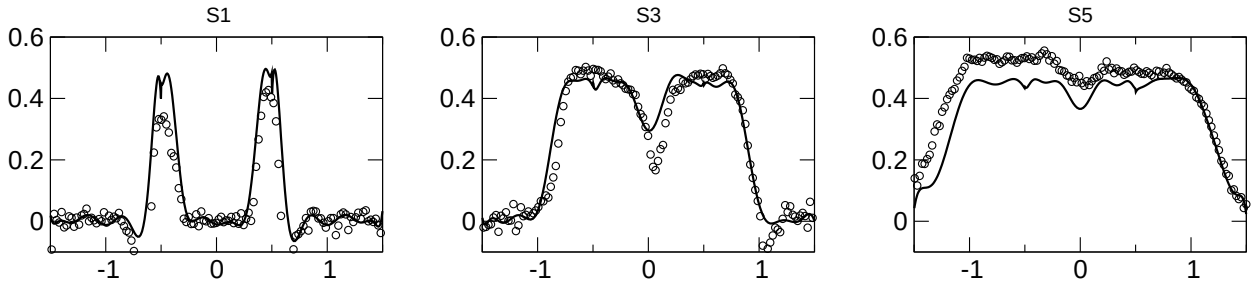

Figure 7: Normalized $< u'c' >$ at the 3 measurement stations. Symbols: experiment; solid line: implicit LES

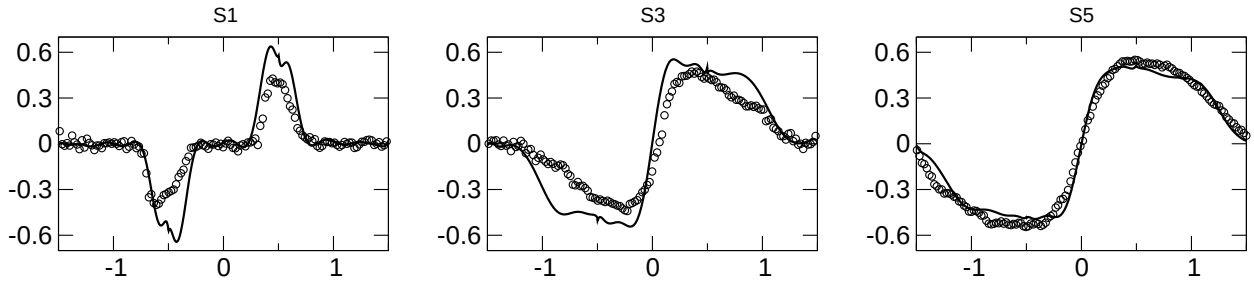

Figure 8: Normalized $< v'c' >$ at the 3 measurement stations. Symbols: experiment; solid line: implicit LES

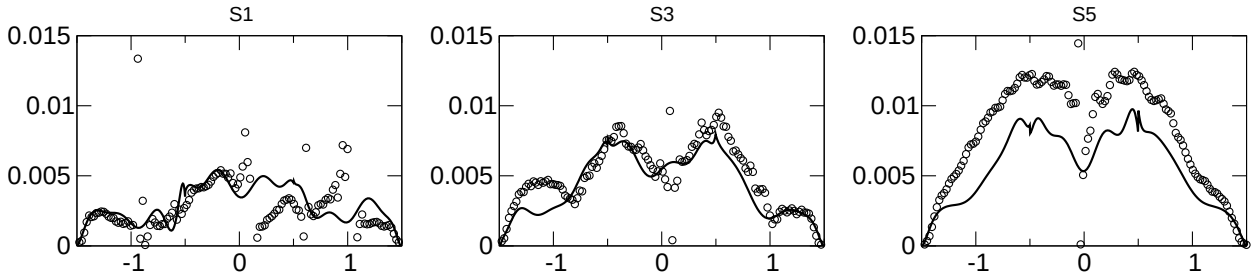

Figure 9: Turbulent viscosity at the 3 measurement stations. Symbols: experiment; solid line: implicit LES

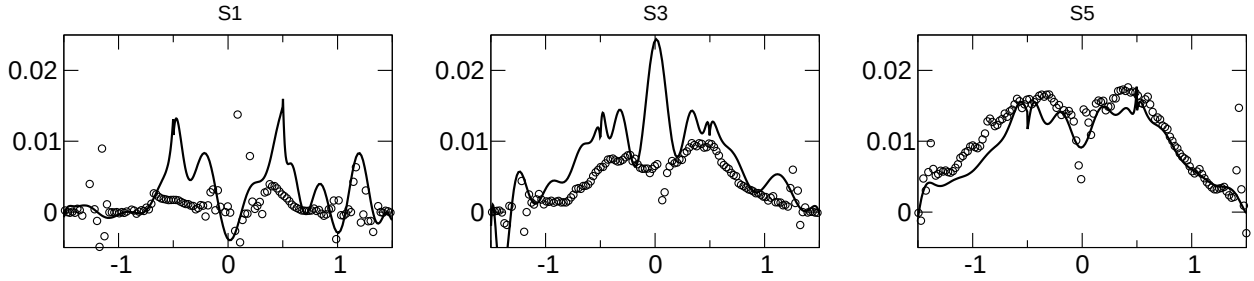

Figure 10: Turbulent diffusivity at the 3 measurement stations. Symbols: experiment; solid line: implicit LES

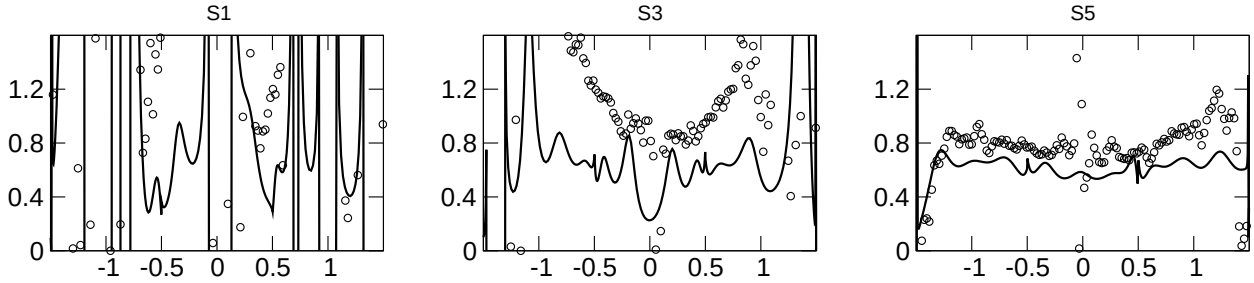

Figure 11: Turbulent Schmidt number at the 3 measurement stations. Symbols: experiment; solid line: implicit LES